Direct Simulation Monte Carlo modelling of the major species in the coma of comet 67P/Churyumov-Gerasimenko

Nicolas Fougere, Kathrin Altwegg, Jean-Jacques Berthelier, Andre Bieler, Dominique Bockelée-Morvan, Ursina Calmonte, Fabrizio Capaccioni, Michael R. Combi, Johan de Keyser, Vincent Debout, et al.

Direct Simulation Monte Carlo modelling of the major species in the coma of comet 67P/Churyumov-Gerasimenko

Nicolas Fougere,[1]★ K. Altwegg,[2] J.-J. Berthelier,[3] A. Bieler,[1] D. Bockelée-Morvan,[3]
U. Calmonte,[2] F. Capaccioni,[4] M. R. Combi,[1] J. De Keyser,[5] V. Debout,[3] S. Erard,[3]
B. Fiethe,[6] G. Filacchione,[4] U. Fink,[7] S. A. Fuselier,[8] T. I. Gombosi,[1] K. C. Hansen,[1]
M. Hässig,[8] Z. Huang,[1] L. Le Roy,[2] C. Leyrat,[3] A. Migliorini,[4] G. Piccioni,[4]
G. Rinaldi,[4] M. Rubin,[2] Y. Shou,[1] V. Tenishev,[1] G. Toth,[1] C.-Y. Tzou,[2]
the VIRTIS and the ROSINA teams

[1]*Department of Climate and Space Sciences and Engineering, University of Michigan, Ann Arbor, MI 48109, USA*
[2]*Space Research and Planetary Sciences, University of Bern, CH-3012 Bern, Switzerland*
[3]*LESIA, Observatoire de Paris, LESIA/CNRS, UPMC, Université Paris-Diderot, F-92195 Meudon, France*
[4]*INAF-IAPS, Istituto di Astrofisica e Planetologia Spaziali, via del fosso del Cavaliere 100, I-00133 Rome, Italy*
[5]*Belgian Institute for Space Aeronomy (BIRA-IASB), Brussels, Belgium*
[6]*Institute of Computer and Netword Engineering, TU Braunschweig, Braunschweig, Germany*
[7]*Lunar and Planetary Laboratory, University of Arizona, Tucson, AZ, USA*
[8]*Department of Space Science, Space Science and Engineering Division, Southwest Research Institute, San Antonio, TX 78238, USA*

ABSTRACT

We analyse the Rosetta Orbiter Spectrometer for Ion and Neutral Analysis (ROSINA) – the Double Focusing Mass Spectrometer data between 2014 August and 2016 February to examine the effect of seasonal variations on the four major species within the coma of 67P/Churyumov-Gerasimenko (H_2O, CO_2, CO, and O_2), resulting from the tilt in the orientation of the comet's spin axis. Using a numerical data inversion, we derive the non-uniform activity distribution at the surface of the nucleus for these species, suggesting that the activity distribution at the surface of the nucleus has not significantly been changed and that the differences observed in the coma are solely due to the variations in illumination conditions. A three-dimensional Direct Simulation Monte Carlo model is applied where the boundary conditions are computed with a coupling of the surface activity distributions and the local illumination. The model is able to reproduce the evolution of the densities observed by ROSINA including the changes happening at equinox. While O_2 stays correlated with H_2O as it was before equinox, CO_2 and CO, which had a poor correlation with respect to H_2O pre-equinox, also became well correlated with H_2O post-equinox. The integration of the densities from the model along the line of sight results in column densities directly comparable to the VIRTIS-H observations. Also, the evolution of the volatiles' production rates is derived from the coma model showing a steepening in the production rate curves after equinox. The model/data comparison suggests that the seasonal effects result in the Northern hemisphere of 67P's nucleus being more processed with a layered structure while the Southern hemisphere constantly exposes new material.

Key words: space vehicles – space vehicles: instruments – comets: general – comets: individual: 67P/Churyumov-Gerasimenko.

"

1 INTRODUCTION

The Rosetta spacecraft has been orbiting comet 67P/Churyumov-Gerasimenko (67P) following its journey around the Sun, providing the first extensive observation of a comet covering a large range of heliocentric distances and geometries. This escort phase enables unprecedented spatial and temporal information about the evolution of 67P and its coma. The evolution of the coma activity falls directly under one of the main science goals of the Rosetta mission: the coma emergence from the surface of the nucleus.

The orbiter carries a suite of 11 instruments combining remote sensing and *in situ* techniques to provide a complete investigation of the comet. The Rosetta Orbiter Spectrometer for Ion and Neutral Analysis (ROSINA) consists of the Comet Pressure Sensor (COPS), the Double Focusing Mass Spectrometer (DFMS), and the Reflectron-type Time-of-Flight mass spectrometer (RTOF). COPS is composed of two gauges that primarily measure the total density and the radial flow, respectively. With its high resolution of $m/\Delta m$ of 3000 at 1 per cent peak height at a mass-to-charge ratio of 28 Da/e, DFMS can measure the elemental and isotopic abundances of the gas species. Finally, the RTOF instrument can provide high time resolution measurements by instantaneously recording the 1–1000 amu mass range (Balsiger et al. 2007; Mall et al. 2016). Also, the Visible and Infrared Thermal Imaging Spectrometer (VIRTIS) combines two different channels: VIRTIS-M takes hyperspectral images of both the nucleus and the coma spanning a range of wavelengths from the UV (0.25 μm) to the near-IR (5.0 μm), while VIRTIS-H is dedicated to high spectral resolution infrared spot spectroscopy (Coradini et al. 2007).

To date, ROSINA has detected many volatile species in the coma of 67P showing abundances rather comparable with measurements in other comets. The exceptions have been CO, early in the mission, and CO_2 that show higher mixing ratios than in most Jupiter Family Comets (Le Roy et al. 2015). Also, ROSINA provided the first detection of molecular oxygen (O_2) in the coma of a comet with abundances ranging from 1 to 10 per cent with respect to water, with a mean value of 3.80, making O_2 the fourth most abundant species in the coma of 67P (Bieler et al. 2015a).

Several instruments on board the Rosetta spacecraft revealed that, similar to comets Hartley 2 (A'Hearn et al. 2011) and Tempel 1 (Feaga et al. 2007), 67P presents a very heterogeneous gas release. During the pre-equinox phase, while the largest flux of H_2O is found in the Northern hemisphere, CO_2 is mostly released from the southern latitudes of the nucleus (Biver et al. 2015; Feldman et al. 2015; Hässig et al. 2015; Fink et al. 2016; Migliorini et al. 2016).

While coma models solely based on solar illumination were able to relatively well reproduce the overall H_2O observations from ROSINA-COPS (Bieler et al. 2015b) and VIRTIS-H (Bockelée-Morvan et al. 2015), these were showing a clear underestimation of the H_2O densities close to the Hapi region. By adding a non-uniform surface activity, Fougere et al. (2016) were able to get a much better agreement with the observations. The model found different activity patterns for different species, which enabled it to capture the heterogeneous pattern for H_2O and CO_2 observed by VIRTIS-M/-H and ROSINA–DFMS from 2014 August to the very beginning of 2015 June (Fougere et al. 2016).

The orientation of 67P's spin axis with a tilt of about 52° results in large seasonal variations. Indeed, the Northern hemisphere is illuminated for a long time when the comet is at large distances from the Sun with rather low energy input, while the Southern hemisphere receives a large amount of energy for a short amount of time (Keller et al. 2015): equinox happened in 2015 May while perihelion was just a few months later on 2015 August 13. This suggests that we may expect differences in the outgassing of the comet before and after equinox when mostly the southern latitudes become illuminated by the Sun. Therefore, a modelling effort to understand the coma of comet 67P after the equinox is required.

First, we present the H_2O, CO_2, CO, and O_2 data derived by DFMS from 2014 August to the end of 2016 February. While Fougere et al. (2016) worked with pre-equinox data, this paper uses a much larger data set covering both pre- and post-equinox, and

will focus mostly on post-equinox model/data comparison. Then, we give a complete description of the Direct Simulation Monte Carlo (DSMC) model with a non-uniform outgassing distribution from the nucleus of 67P following the method used in Fougere et al. (2016). Then, we show a comparison between the DSMC model and the measurements from DFMS and VIRTIS-H (Bockelée-Morvan et al. 2016). The final section is dedicated to a discussion notably with the evolution of the production rate for the four major species of the coma of comet 67P.

2 DESCRIPTION AND ANALYSIS OF THE ROSINA–DFMS DATA

Most of the results presented in this paper are resulting from the measurements from both ROSINA and VIRTIS. A complete description of the VIRTIS-H raster images and column density measurements can be found in Bockelée-Morvan et al. (2016). The ROSINA–DFMS data that we use for constraining our coma model present new measurements that have not been previously analysed.

While the DFMS instrument can measure both neutral and ion abundances using a Nier–Johnson configuration where a 90° radial electrostatic energy analyser is combined with a 60° magnetic deflection (Balsiger et al. 2007; Johnson & Nier 1953), for the purpose of this study, we are only interested in the neutral observations. As they enter the instrument, the neutrals are bombarded by 45 eV electrons and a fraction of them are positively ionized and/or break up in ionized fragments. These ions are then accelerated and hit a detector made of two rows of 512 pixels along the dispersive axis.

Even though the DFMS has a high-mass resolution ($m/\Delta m \approx 3000$ at the 1 per cent peak level), peaks in spectra are often not completely separated. Hence, a Gaussian fitting is used to evaluate the contribution from each species to the total peak providing the relative abundances of the different species. For the four major species, the contributions from other species are marginal and can be neglected. Our analysis uses the fragmentation patterns and sensitivity values determined during the calibration campaign with the flight spare model of DFMS.

Finally, even after spending a decade in space, the Rosetta spacecraft releases gas and its contribution was characterized before arriving at 67P and is subtracted from the determined DFMS signal (Schläppi et al. 2010).

In this study, the number densities for all species and from COPS are linearly interpolated to the time stamps of the H_2O measurements. This interpolation takes the closest measurement in time before and after the H_2O time stamp. We only keep the points when the four major coma species (H_2O, CO_2, CO, and O_2) are detected on both DFMS channels within 90 min around the window for a total of about 21 000 data points from 2014 August 4 to 2016 February 29, while Fougere et al. (2016) kept all DFMS points even when one of these majors species was not detected. The sums of the relative abundances of these four species are constrained so that they fit the calibrated total gas density measured by COPS for every measurement, which is also different from the data set used in Fougere et al. (2016) that was only globally rescaled to COPS. The approach used in the current paper enables us to obtain the most reliable species' densities from the DFMS/COPS instruments. The resulting full data set is presented in Fig. 1 together with the comet's heliocentric distance and the spacecraft's cometocentric distance.

The ROSINA data showed that the density evolution of H_2O and CO_2 with time presented the same signs of
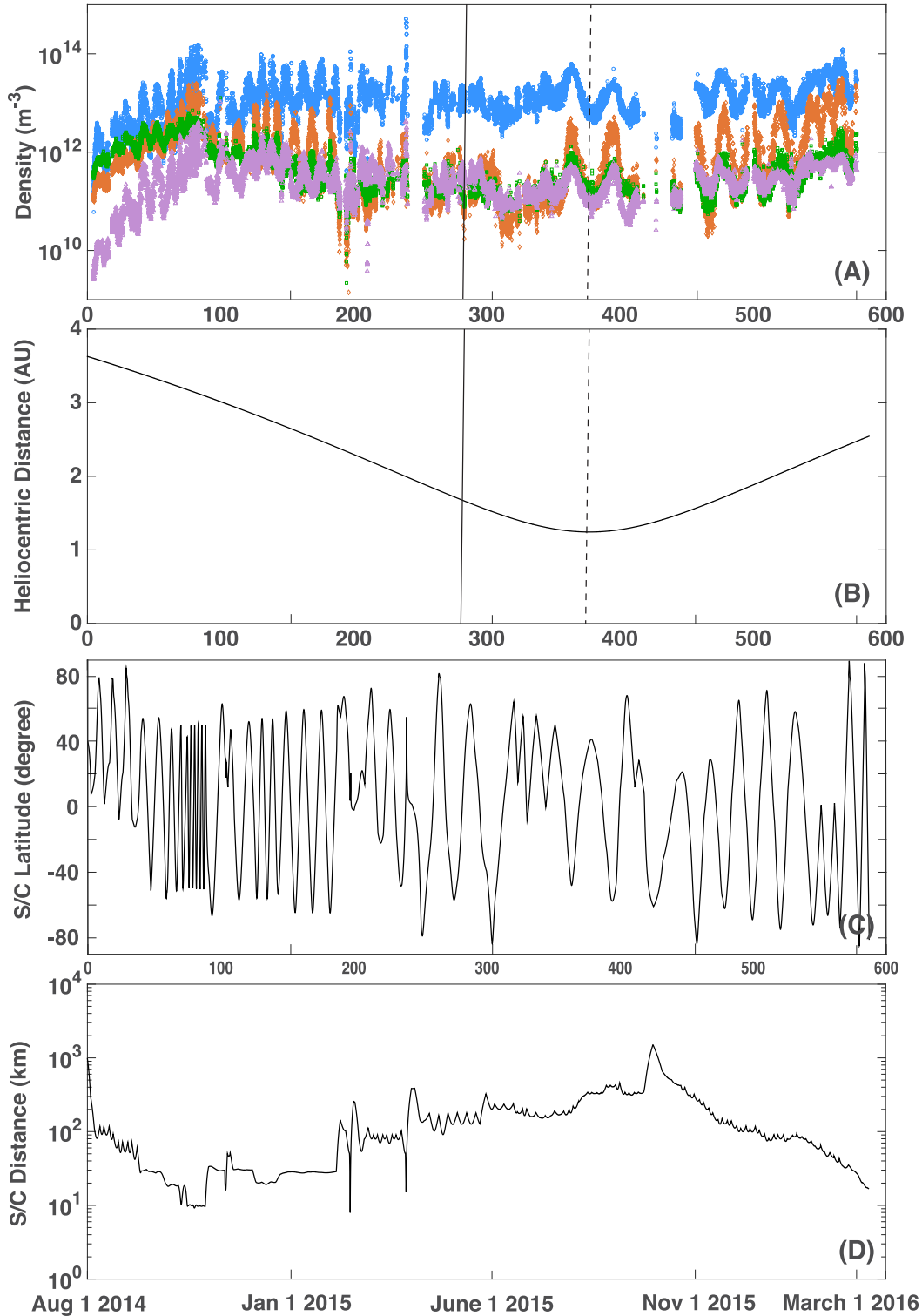
Figure 1. Panel A: H$_2$O (blue), CO$_2$ (orange), CO (green), and O$_2$ (purple) number densities observed by the DFMS instrument from 2014 August 4 to 2016 February 29. Panel B: distance between the comet and the Sun in au. Panel C: spacecraft latitude in degrees. Panel D: spacecraft cometocentric distance in km. The vertical dashed line and solid line represent the time of perihelion and equinox, respectively.

anti-correlation (Pearson) pre-equinox with both RTOF (Mall et al. 2016) and DFMS (Hässig et al. 2015; Fougere et al. 2016). Within the scale of a few days, with the motion of the spacecraft, when H$_2$O presented a local maximum, CO$_2$ would show a local minimum and

vice versa (Fig. 2). Also, DFMS showed a strong correlation between H$_2$O and O$_2$ with a correlation of 0.88 for data between 2014 September and 2015 March (Bieler et al. 2015a). Post-equinox, the relative behaviour of the four species of interest changes due to a
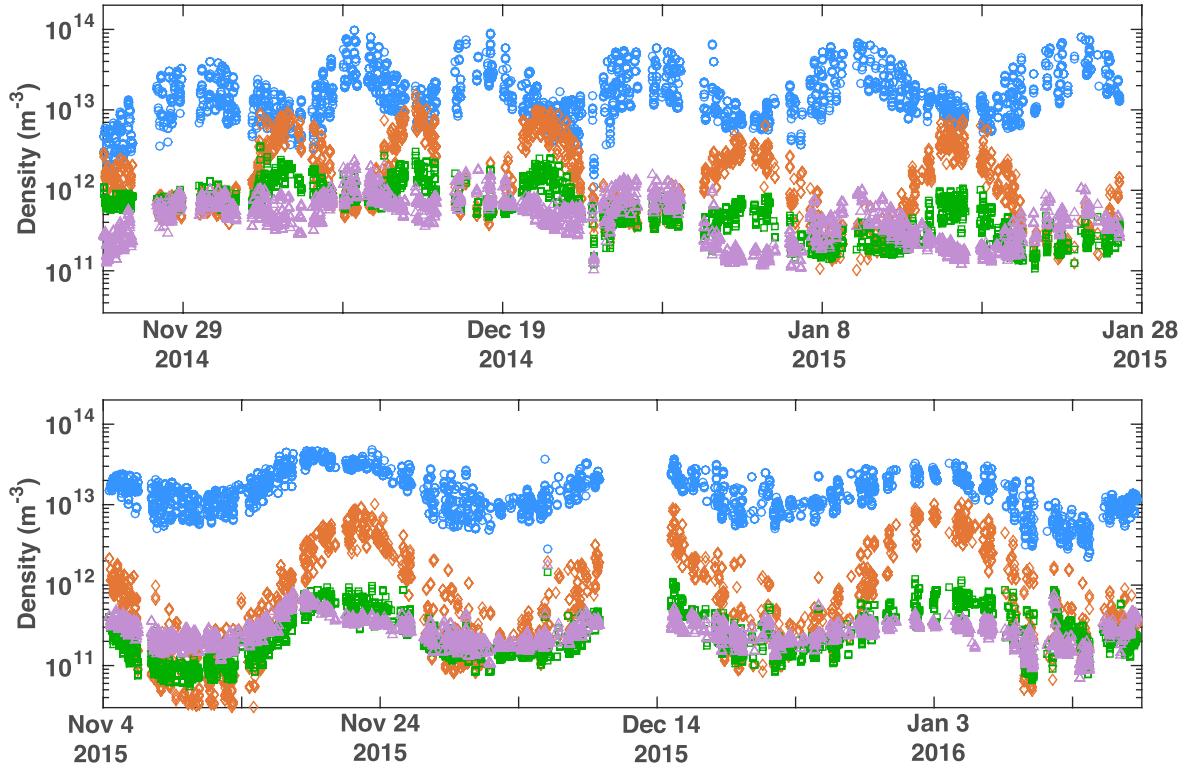
Figure 2. H₂O (blue), CO₂ (orange), CO (green), and O₂ (purple) number densities observed by the DFMS instrument between 24 November 2014 and 28 January 2015 (top panel), and between 2015 November 4 and 2016 January 18 (bottom panel). The relative behaviour of the different species is dramatically different pre- and post-equinox.

seasonal effect with the Southern hemisphere getting most of the solar energy input, and the evolution with time of H₂O, CO₂, CO, and O₂ becomes well correlated (Fig. 2).

To illustrate this phenomenon more quantitatively, Fig. 3 shows the H₂O density as a function of CO₂, CO, and O₂ before and after equinox. The correlation between CO₂ and H₂O went from a value of 0.08 pre-equinox to a value of 0.68 post-equinox. Similarly, CO and H₂O have their correlation increase from 0.16 to 0.78. Finally, O₂ stays well correlated throughout, at a value of 0.81.

3 MODEL OF THE COMA OF 67P

Most of the practical applications of coma studies require the consideration of rarefied gas flows where collisions are not sufficient to sustain the local thermodynamic equilibrium so that a classical hydrodynamics approach is not valid. Hence, a kinetic method is necessary to accurately compute the gas flow in the coma since it is valid for all ranges of Knudsen numbers expected in the coma of the comet.

The evolution of the phase-space distribution function of species s (F_s) is determined by the flow of particles under the influence of external forces and by the net effect of collisions leading to the Boltzmann equation (Schunk & Nagy 2009):

$$\frac{\delta F_s(\boldsymbol{r}, \boldsymbol{v}_s, t)}{\delta t} = \frac{\partial F_s(\boldsymbol{r}, \boldsymbol{v}_s, t)}{\partial t} + (\boldsymbol{v}_s.\nabla_{\boldsymbol{r}})F_s(\boldsymbol{r}, \boldsymbol{v}_s, t)$$
$$+ (\boldsymbol{a}_s.\nabla_{\boldsymbol{v}_s})F_s(\boldsymbol{r}, \boldsymbol{v}_s, t), \qquad (1)$$

where $\boldsymbol{r}$ is the position vector, $\boldsymbol{v}_s$ the velocity vector, $\boldsymbol{a}_s$ the acceleration vector and t the time. The left-hand side $\delta F_s/\delta t$ is the integral of collisions that account for interparticle interaction.

Today analytical solutions or even direct numerical solutions to the Boltzmann equation are only possible for special cases. Otherwise, particle simulation approaches are normally used. The DSMC method (Bird 1994) is one of the most used approaches to find a numerical solution to the Boltzmann equation. Such an approach has been applied to the cometary coma for several decades (Combi 1996); in this paper, we use the Adaptive Mesh Particle Simulator (AMPS) code (Tenishev, Combi & Davidsson 2008; Tenishev, Combi & Rubin 2011; Fougere et al. 2013) to model the coma of comet 67P. First implemented to run using a 2D axisymmetric configuration, the AMPS coma model was adapted and tested in 3D, which enabled the use of irregular nucleus shapes (Fougere 2014). Originally, the gas flux was solely determined from the local illumination of every single surface facet derived from a triangulated nucleus mesh including self-shadowing, i.e. every part of the nucleus was assumed equally active under the same illumination conditions (Fougere 2014; Bieler et al. 2015b; Bockelée-Morvan et al. 2015). Since then, the inclusion of surface activity distributions (i.e. a variation in the response of specific surfaces to solar illumination) enabled the model to match much better the observations from the ROSINA and VIRTIS instruments (Fougere et al. 2016).

3.1 Determination of the activity distribution

We follow the approach mentioned in Fougere et al. (2016) to describe the surface activity distribution using a spherical harmonic expansion with the use of 25 terms (i.e. up to the order of 4). The coefficients of the spherical harmonic expansion are found by minimizing the square of the differences between an analytical model and the DFMS data set from 2014 August to the end of
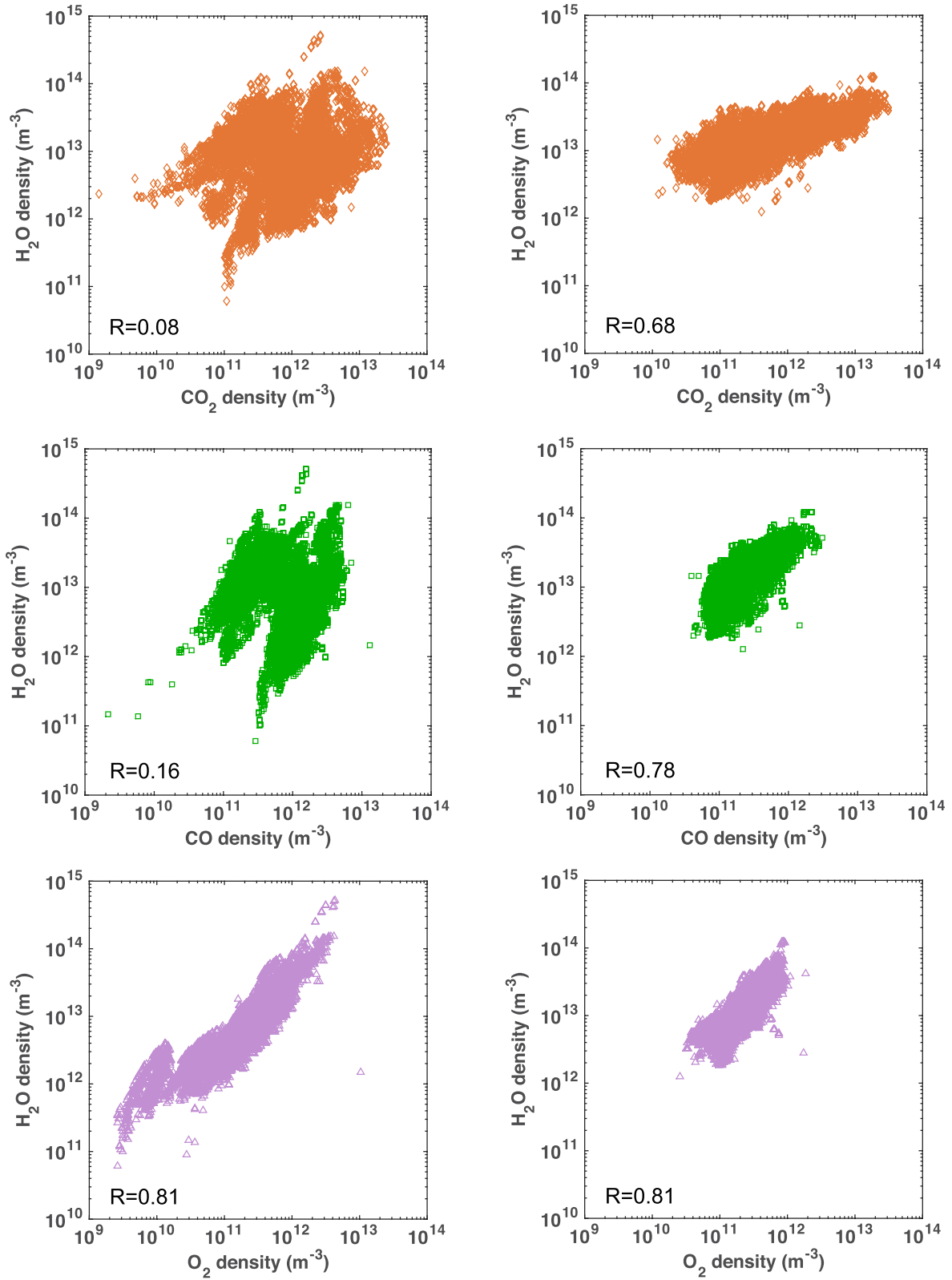
Figure 3. H_2O density as a function of the CO_2 density (top panels), CO density (middle panels), and O_2 density (bottom panels) comparing pre- (left) and post-equinox (right), showing clear increase in the correlation of these species with H_2O between pre- and post-equinox.

2016 February for each species. We refer the reader to Fougere et al. (2016) for details of the method to derive these.

The approach requires to solve a problem as follows:

$$\min_{x \in \mathbb{R}^N} ||Cx - \boldsymbol{d}||_2^2, \qquad (2)$$

where $\boldsymbol{d}$ is a vector of size M, the length of the DFMS data set (number of data points $\sim$21 000 per species), x is the objective function representing the coefficients of the spherical harmonic expansion of size $N = 25$, and **C** is an $M \times N$ matrix defined as follows:

$$C_{ij} = \frac{1}{R_{au}^\beta} \left(\sum_{k=1}^{N_{facets}} \frac{(g(\Theta_k))_i \, S_k \, (\cos(\alpha_k))_i}{r_k^2} Y_j(\vartheta_k, \varphi_k) \right), \qquad (3)$$

where N_{faces} is the total number of triangles of the nucleus surface mesh, β is the exponent of the power law with R_{au}, the function g is defined similarly as in Bieler et al. (2015b) by the following equation:

$$g(\Theta_{SZA}) = \max(a_{night}, \cos(\Theta_{SZA})), \qquad (4)$$

where the value a_{night}, which corresponds to the flux ratio for a given location between conditions at local noon, i.e. when the triangle is directly oriented towards the Sun, and on the night side, is enforced when the triangle is in shadow. The surface area of the kth triangle is S_k; r_k and α_k are the distance and angle between the spacecraft and the kth triangle, respectively. The parameter ϑ_k and φ_k are the colatitude and longitude of the centre of the kth triangle from the nucleus model, respectively. Finally, the Y_js represent the different terms of the spherical harmonics.

This analytical model requires definition of two parameters: the exponent corresponding to a power law of the evolution with heliocentric distance β and the ratio between the flux for a triangle when it is in shadow with respect to the Sun when it is in the zenith a_{night}. In order to get an a priori estimate of the β parameter, we applied a best fit of the evolution of the number density from all the DFMS data set times the spacecraft distance from the comet squared (Fig. 4). This is only a very rough estimate since it does not take into account the coma asymmetry and the evolution of the velocity as the comet approaches the Sun and leads to uncertainties in the slope of $\sim\pm 0.5$ (Hansen et al. 2016). Also, it does not take into account any difference of the evolution with heliocentric distance before and after perihelion. However, some testing showed that such variations in the β parameter would not change drastically the retrieved surface activity distribution, and we find that some of those variations come naturally out of the seasonal effect of changing solar illumination geometry. We find that the values 5.6, 2.8, 2.6, and 4.9 fit best for H_2O, CO_2, CO, and O_2, respectively. The a_{night} parameter was picked to be 2 per cent for H_2O and CO_2 and 10 per cent for CO and O_2 due to their much lower sublimation temperature. These parameter values are summarized in Table 1.

Fig. 5 shows a comparison between the analytical model best fit and the DFMS data. The correlations are 0.89, 0.88, 0.73, and 0.77 for H_2O, CO_2, CO, and O_2, respectively. The model is able to capture the changes in the relative behaviour of the density evolution for the different species before and after equinox. It appears that the analytical model underestimates the CO_2 and CO densities for the first two months (2014 August and September), and the CO_2, CO, and O_2 densities close to perihelion. These differences are due to the simplistic character of a single power law to describe the evolution of the production rate for such an extended period of time. To correct these variations, we will add a multiplying coefficient λ to the flux in the boundary conditions of the DSMC simulations.
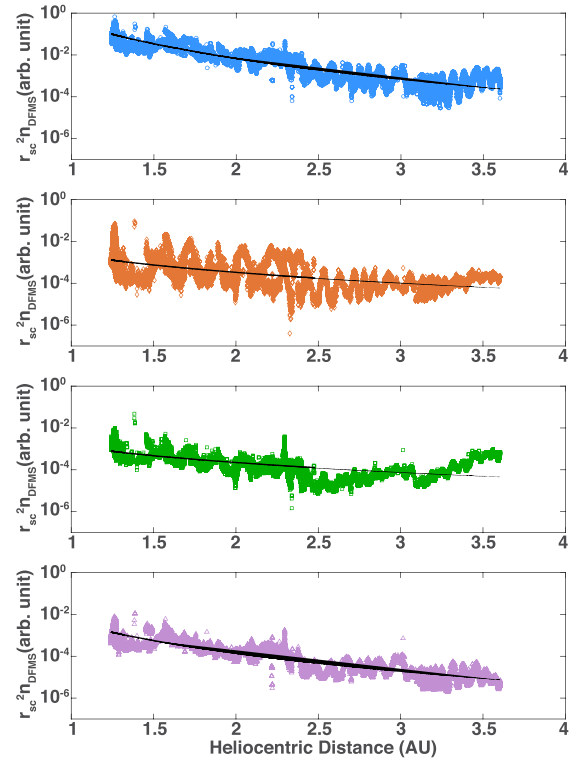

Figure 4. Best fit of the evolution of the number density from DFMS (pre- and post-equinox) times the spacecraft distance squared from the comet in arbitrary units for H_2O (blue), CO_2 (orange), CO (green), and O_2 (purple) in a function of heliocentric distance, and the corresponding best-fitting power laws with exponents -5.6, -2.8, -2.6, and -4.9, respectively, which give a priori values for parameter β.

Table 1. Parameters used in the analytical model to compute the surface activity distribution.

Species	β	a_{night}
H_2O	5.6	2 per cent
CO_2	2.8	2 per cent
CO	2.6	10 per cent
O_2	4.9	10 per cent

The resulting surface activity distributions are represented in Fig. 6. We notice that the H_2O surface distribution is similar to the one that was deduced from using pre-equinox data only (Fougere et al. 2016). It is also the case for CO_2, which still shows a stronger activity in the southern latitudes. However, the new CO_2 retrieval does not show any enhancement in the Hapi region of the nucleus which the VIRTIS comparison from Fougere et al. (2016) showed to be more important than in the observations in the pre-equinox study. This suggests that the general activity of the comet is mainly changing with time due to the illumination pattern evolving with the relative position between the Sun and the nucleus. The O_2 surface activity distribution is similar to H_2O as expected from their obvious correlation. Finally, CO shows a more spread out activity with some enhancements both in the 'neck' and southern latitude regions.

3.2 DSMC simulations of the coma

The inner boundary is defined by the temperature from the thermophysical model of Davidsson & Gutierrez (2004, 2005, 2006)
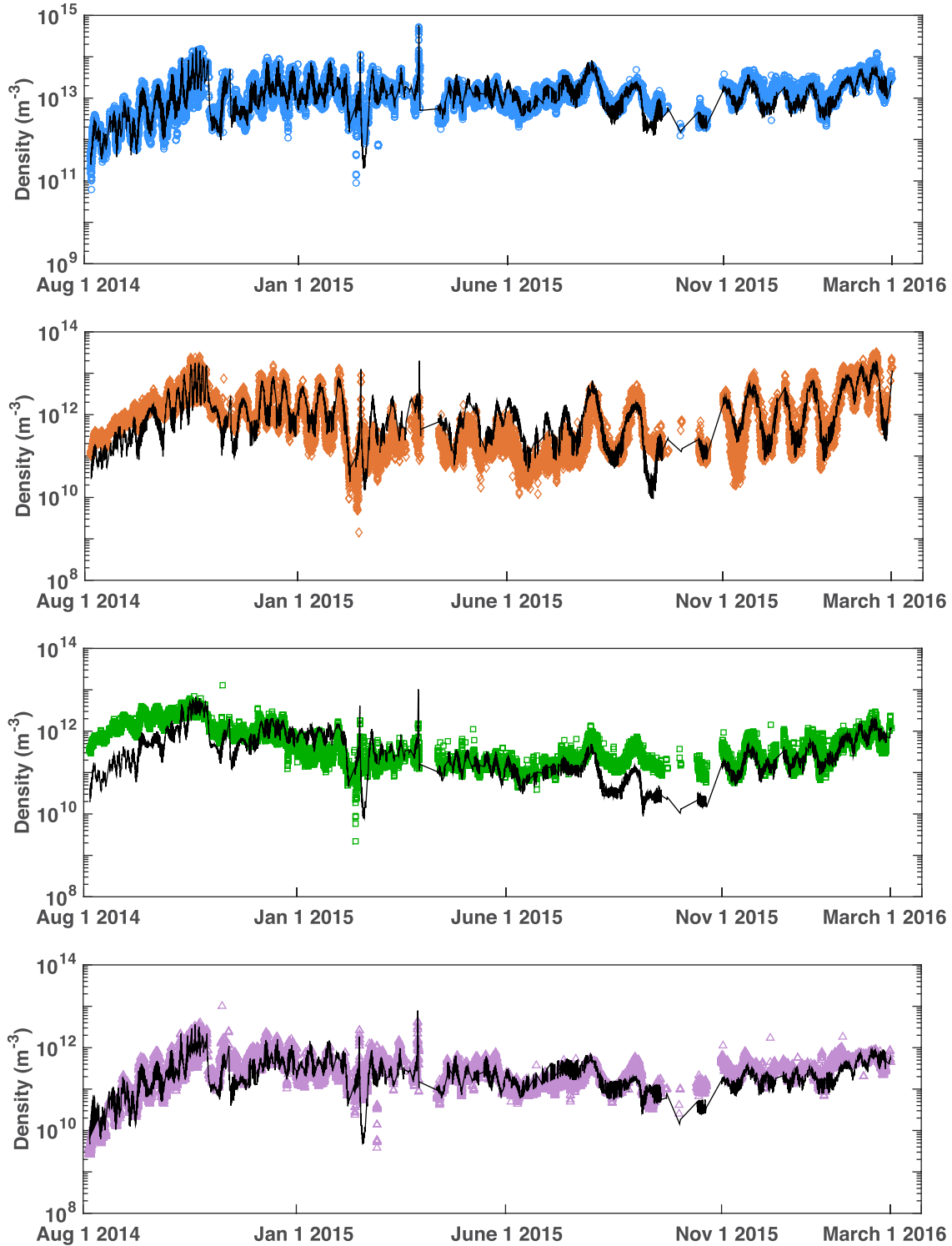
Figure 5. Best fit of the DFMS number density from the analytical model (solid line in black) for the ROSINA measurements H_2O (blue), CO_2 (orange), CO (green), and O_2 (purple).

depending on the solar direction with respect to the kth nucleus facet and the gas flux is computed by:

$$F_k = \lambda \frac{G\left(\Theta_{SZA}\right) f_k}{R_{au}^{\beta}}, \tag{5}$$

where f_k is deduced from the activity mapping presented in Fig. 6. λ is a multiplying factor, different for each species and each set of

simulations, to correct the discrepancies from the power-law approximation of the evolution of the gas production rate with the heliocentric distance. The function $G(\Theta_{SZA})$, simulating the variation of the flux with solar zenith angle similarly to the simulations presented in Bieler et al. (2015b), is defined by

$$G\left(\Theta_{SZA}\right) = a_{night} + \left(1 - a_{night}\right) \cos\left(\Theta_{SZA}\right). \tag{6}$$
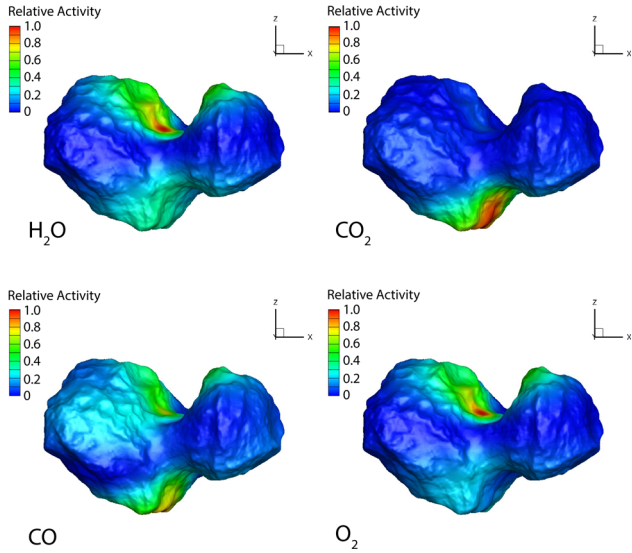
Figure 6. Surface activity distribution for the species H_2O, CO_2, CO, and O_2. The maps will be used in addition to the local illumination to derive the gas flux at the inner boundary conditions for each case of the DSMC simulations.

Table 2. Geometries for which the DSMC simulations were performed. For each of the days in the table below 12 simulations were run with a time resolution of an hour corresponding to a nucleus rotation. Some of the cases have been rescaled and extrapolated to post-perihelion.

Date	R_{au} (au)	Sun latitude (°)	Extrapolated date
08-23-2014	3.5	43	x
12-23-2014	2.7	32	x
03-04-2015	2.2	20	x
05-06-2015	1.7	1.5	x
06-08-2015	1.5	−13	01-14-2016
07-01-2015	1.35	−25	12-01-2015
07-22-2015	1.27	−38	10-28-2015
08-16-2015	1.24	−49	09-25-2015

The self-shadowing of the nucleus is taken into account, and $G = a_{night}$ when a facet is in the shadow.

The DSMC approach is computationally expensive so that we can only run a reasonable number of simulations. We decided to run eight sets of multi-species simulations with the different species collisionally coupled, each corresponding to a different day pre-perihelion spanning the solar latitude range. For each set of simulations, we ran 12 cases with a resolution of an hour to cover one rotation of the nucleus [from 12.4 h to 12 h (Mottola et al. 2014)]. Some of these cases were rescaled post-perihelion to a date with similar subsolar latitudes and longitudes. These add up to a total of 144 output data files per species. The details of the dates and geometries used in the simulations can be found in Table 2.

By extracting the density at the position of the spacecraft every hour from the set of cases with the closest date with respect to the time of interest with a resolution, and then picking the case with the closest solar longitude, we can extrapolate the model values from 2014 August to 2016 February (Fig. 7). We notice that the model follows well the DFMS data for the four species considered in this study for the entire 18 month period. Hence, keeping a constant surface activity distribution and solely changing the Sun–nucleus

geometry reproduce the DFMS data both pre- and post-equinox, capturing the changes in the relative behaviour of the different species.

Fig. 8 shows the diurnal variation of the density of the four species of interest for two weeks pre-equinox and a period of 10 d post-equinox. It appears that the diurnal evolution of H_2O and O_2 is relatively well followed by the model while CO_2 shows a better agreement with the data before equinox. Finally, the amplitude of the oscillations for CO in the model is larger than those observed by DFMS.

4 COMPARISON OF THE MODEL WITH VIRTIS OBSERVATIONS

The measurement technique used by VIRTIS, being a remote sensing instrument, is different than the one used by ROSINA, *in situ*. Hence, a comparison between the observations of these two instruments is not straightforward. The use of a coma model as a tool to do so is one possible approach. Moreover, the two instruments sample gases in different parts of the coma with ROSINA measuring the gas properties at the spacecraft location most of the time at the terminator, whereas VIRTIS probes molecules close to the nucleus in different directions. Hence, the use of the two data sets should provide better constraints to the outgassing. The pre-equinox model was compared to the VIRTIS-M images from the month of April from Migliorini et al. (2016) and the VIRTIS-H observations from 2014 November to 2015 January from Bockelée-Morvan et al. (2015) showing good agreement (Fougere et al. 2016). VIRTIS coma observations were also performed post-equinox (Bockelée-Morvan et al. 2016) enabling us to perform a model/data comparison during that time period.

4.1 Qualitative comparison with the raster images from VIRTIS-H

VIRTIS-H performed some extended observations to probe the coma and obtain a spatial distribution of the coma. Bockelée-Morvan et al. (2016) reported brightness distributions of the 2.7 μm H_2O band and the 4.26 μm CO_2 band for two different observation periods: on 2015 July 30 from 17:38:59 to 21:14:58 UT, and from 2015 August 8 at 20:52:23 UT to 2015 August 9 at 00:23:52 UT. These intensity images suggest that both H_2O and CO_2 are mostly released from the southern latitudes of the nucleus, which is drastically different from the results of coma mappings with VIRTIS-M from pre-equinox data that were showing H_2O mostly from the 'neck' area well correlated with the local illumination and CO_2 (Fink et al. 2016; Migliorini et al. 2016).

The model presented in this paper gives access to a full distribution of the density in the coma so that it can be integrated along the VIRTIS line of sight derived from NAIF SPICE. We used the geometry of the median time for both these observations and computed the column densities (Fig. 9). Due to the high gas production rates, the bands become optically thick, notably with attenuations up to almost a factor of 9 for the CO_2 ν_3 band (Bockelée-Morvan et al. 2016), and a simple *g*-factor cannot be used to convert the intensity maps from Bockelée-Morvan et al. (2016) to column densities. Moreover, the high asymmetry of the coma and the optical thickness of these bands in the emitted radiation make the use of approximations such as the escape probability method (Bockelée-Morvan 1987) not rigorously applicable. Hence, a quantitative comparison would require modelling of the opacity using a full
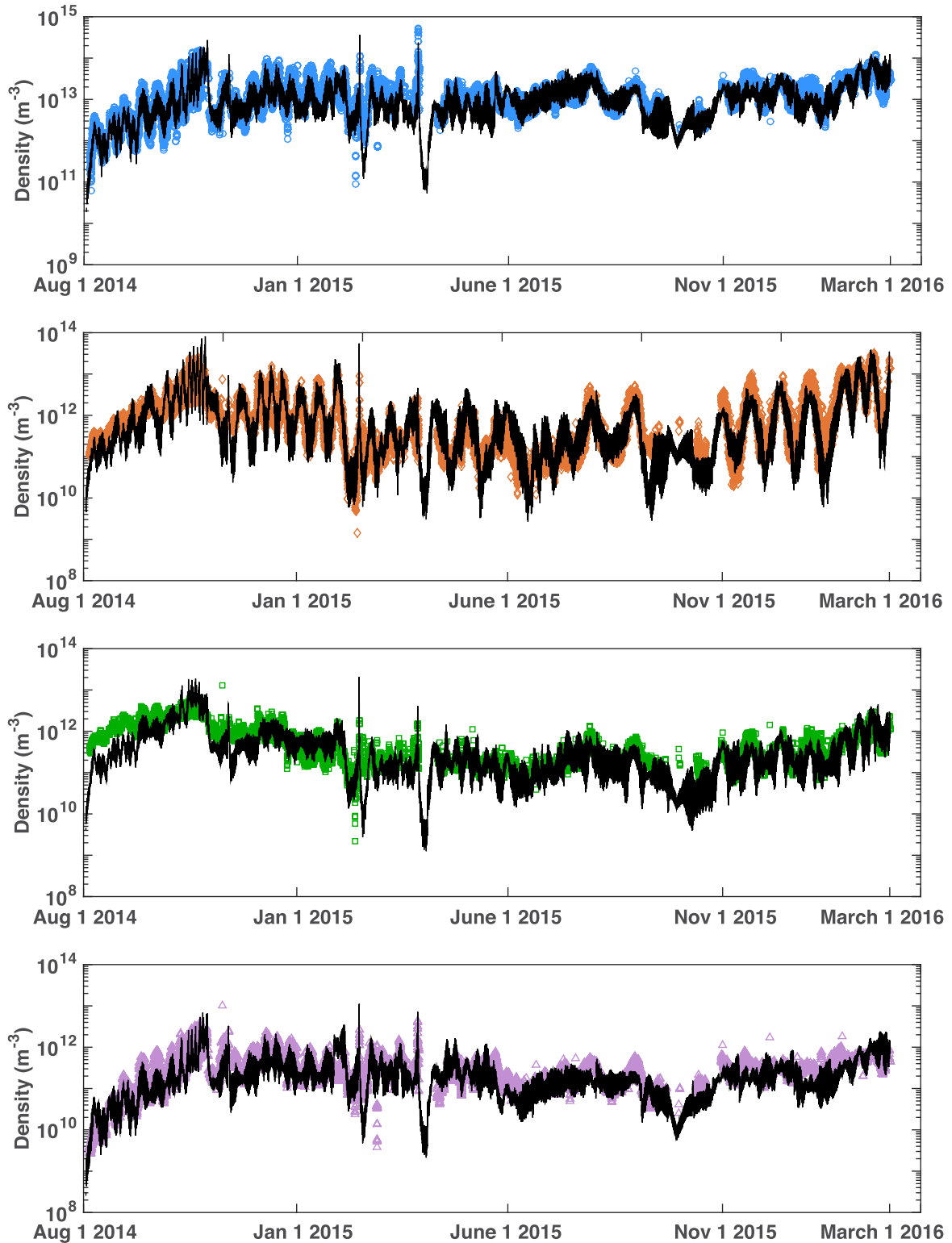
Figure 7. Densities extracted at the location of the spacecraft from the DSMC model (solid line in black) compared to the ROSINA data for H_2O (blue), CO_2 (orange), CO (green), and O_2 (purple).

radiative transfer model as in Debout, Bockelée-Morvan & Zakharov (2016), which is outside of the scope of this paper. However, a qualitative comparison is possible.

For both observation times, the model suggests that both H_2O and CO_2 are mostly produced from the southern latitudes of the

nucleus. Also, the model suggests that the CO_2 fan is narrower than the H_2O fan. Those are in agreement with the VIRTIS-H raster image observations from Bockelée-Morvan et al. (2016) confirming the fact that the solar illumination is at the origin of this change of behaviour going through equinox.

Figure 8. Diurnal evolution of the number density for H_2O (blue), CO_2 (orange), CO (green), and O_2 (purple) from the ROSINA data (symbols) compared with the DSMC model (solid lines). To clarify the plot and avoid overlapping, the CO_2 densities were divided by factors of 20 and 200, and CO by factors of 400 and 3000 in the top and lower panels, respectively.

4.2 Quantitative comparison with the column densities deduced from the VIRTIS-H measurements

In order to estimate the column densities deduced from the brightness VIRTIS-H measurements without using a full radiative transfer model, Bockelée-Morvan et al. (2016) focused on the analysis of the 4.45–5.0 μm range presenting emissions from the $\nu_3-\nu_2$ and $\nu_1-\nu_2$ H_2O hot bands, and the ν_3 $^{13}CO_2$ band extending from 4.35 to 4.42 μm. The data cover a time range from 2015 July 8 to 2015 September 27 showing the evolution of the species column densities with perihelion passage. Also other volatiles such as OCS and CH_4 were detected by VIRTIS during this time period (Bockelée-Morvan et al. 2016) but we model only the four major species here.

Using the Rosetta trajectory and attitude from SPICE, we can compute the modelled column density for the times of observation. Fig. 10 shows the column densities observed by the VIRTIS-H instrument as a function of the modelled column densities for H_2O and CO_2, assuming that the ratio $CO_2/^{13}CO_2 = 89$ (Bockelée-Morvan et al. 2016). The correlation factors between the column densities from VIRTIS-H and from the model are 0.68 and 0.72 for H_2O and CO_2, respectively. The CO_2 column densities observed by VIRTIS-H are relatively well reproduced by the model. The H_2O column densities from the model had to be multiplied by a factor of 0.25 to get in the range of the VIRTIS-H column densities. While an overestimation of the model of the observations by a factor of a few is possible on rare occurrences, it appears in this case that the general data set is overestimated by the model. These observations are taken near perihelion when the spacecraft was located at large distances from the nucleus between 150 and 1057 km. Hence, the *in situ* measurement from ROSINA measures the coma at large distances from the nucleus while VIRTIS-H probes the very inner coma with pointing closest distances from 2.69 to 6.88 km (Bockelée-Morvan et al. 2016). The choice of the case with the closest geometry may not be sufficient to capture the rapidly changing coma that close to perihelion. Also, the assumption of active Sun used in the simulations for the photodissociation rates using the higher values from Huebner, Keady & Lyon (1992) can induce an error of about 10 per cent, but it is not sufficient to explain this factor of 4. It is possible that the rather large uncertainty of H_2O outgassing pattern from the nucleus surface deduced in Section 3 leads to a surface activity not broad enough resulting in higher values for the column densities from the model. Another explanation may reside in the release of H_2O in the coma not being solely due to the direct sublimation of the nucleus but by the addition of the contribution of some sublimating icy grains, which is not treated in this model. Such a distributed source can release H_2O particles at extended distances from the nucleus, which could explain the difference observed between the two instruments. However, a more detailed study that is outside the scope of this paper needs to be conducted to validate this conjecture. We refer the reader to the Discussion section for an additional analysis of this difference between the model based on the ROSINA measurements and the VIRTIS-H observations.

5 DISCUSSION

The DFMS data show a clear difference in the relative behaviour of the species considered in this study, with the main species H_2O, CO_2, CO, and O_2 becoming well correlated after equinox. Similar observations were done comparing the VIRTIS-M images from
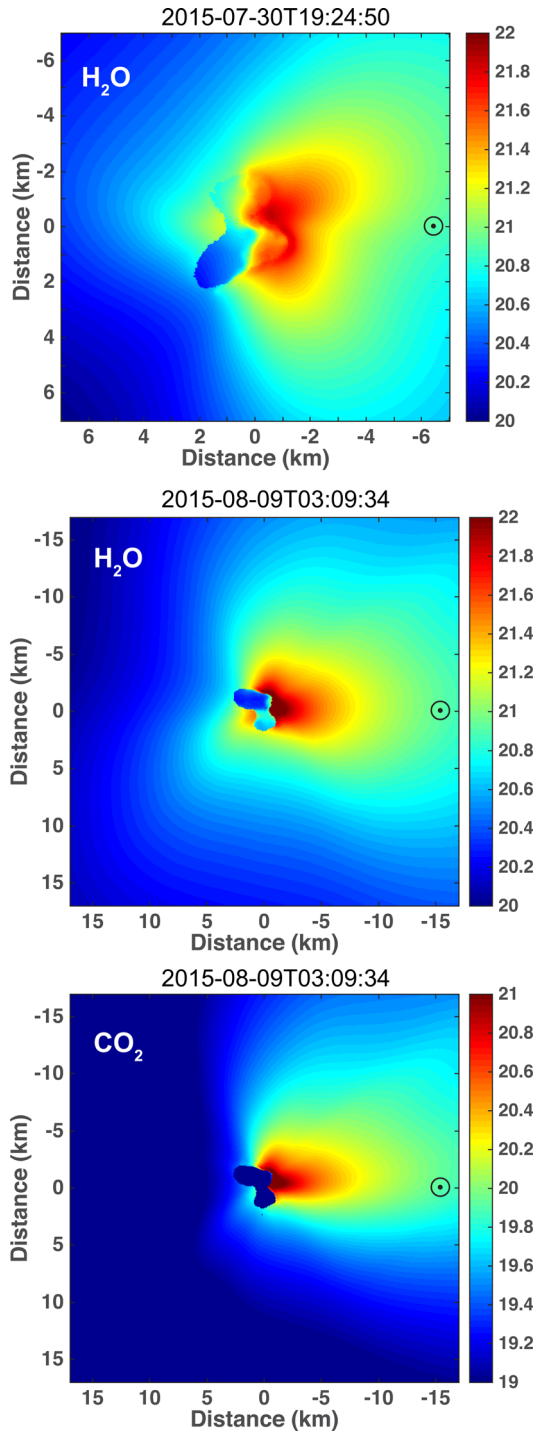
Figure 9. $\log_{10}$ of column densities (m^{-2}) computed from the case with the closest geometry of the median time of the raster images from VIRTIS-H presented in Bockelée-Morvan et al. (2016).

2015 April (Fink et al. 2016; Migliorini et al. 2016) to the VIRTIS-H raster images from 2015 July to 2015 August (Bockelée-Morvan et al. 2016). However, the surface activity distributions for H_2O and CO_2 from the nucleus are similar to the ones when only constrained by pre-equinox data. Hence, the general changes in the observed gas flux of the comet are attributed to the illumination variations as the relative position between the nucleus and the Sun evolves, and not to a temporal change of the state of the nucleus.

Figure 10. VIRTIS-H column densities deduced from observation times ranging from 2015 July 8 to 2015 September 27 (Bockelée-Morvan et al. 2016) as a function of the model column densities for H_2O and CO_2. The model H_2O column densities were applied a factor of 0.25 to match the data range.

The comet activity distribution (Fig. 6) can be interpreted as the strong seasonal variations created by different illumination conditions between the Northern and Southern hemispheres of the nucleus. The Southern hemisphere receiving large amounts of solar energy for a short amount of time presents a vigorous activity that erodes the surface so that fresh material is emitted. While the Northern hemisphere, illuminated for a much longer time but at larger distances from the Sun, receives rather weak energy inputs, which preferentially depletes the somewhat deeper layers of ice from the more volatile species such as CO_2. Thus, the Northern hemisphere of 67P's nucleus should be more 'evolved' and presents more of a traditional layered structure of material than in the Southern hemisphere. This general structure is in agreement with the quasi-3D thermal model from De Sanctis et al. (2010), which shows that the activity pattern of 67P is strongly influenced by the direction of the poles. In the Southern hemisphere of the nucleus, due to fast erosion of the external layers containing dust and H_2O, the CO and CO_2 ice levels come near the comet surface leading to a region of enhanced flux relative to these species (De Sanctis et al. 2010). Also, the evidence of brightening and blueing of the surface at smaller heliocentric distances from the VIRTIS-M images indicates the presence of more ice closer to the surface in the upper layers supporting the idea of fresh material in the Southern hemisphere (Filacchione et al.
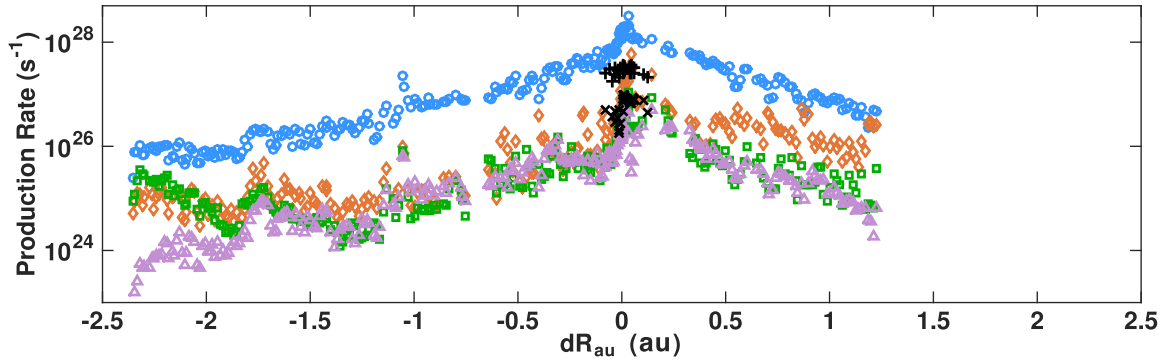
Figure 11. Evolution of the production rate for the species H_2O (blue), CO_2 (orange), CO (green), and O_2 (purple) from the DFMS data using the DSMC model to take into account the asymmetry of the coma and the evolution of the velocity as a function of heliocentric distance with respect to the closest approach (1.24 au) dR_{au} using the definition that dR_{au} is negative before perihelion and positive after perihelion. The black plus and cross symbols represent, respectively, the H_2O and CO_2 production rates deduced from the VIRTIS-H observations using the DSMC model.

2016a). Furthermore, VIRTIS-M has detected the presence of surface CO_2 ice in an area of the Anhur region exiting from the winter hemisphere, which has completely sublimated and disappeared in less than one month (Filacchione et al. 2016b).

Similarly, as in Fougere et al. (2016), the use of a model can enable us to accurately compute the gas production rate of the comet observed by the instruments on board the Rosetta spacecraft without any assumption of symmetry or constant gas velocity in the coma. To do so, we extract the density from the model at the time of the ROSINA observation, and compute the ratio between the corresponding observed and modelled densities, which then constitutes the correcting factor to apply to the computed gas production rate from the model. Then, we take the average over a period of 2 d to decrease the noise. Fig. 11 illustrates the evolution of the H_2O, CO_2, CO, and O_2 production rates with respect to the heliocentric distance from the closest approach distance at perihelion (1.24 au) dR_{au} using the definition that dR_{au} is negative before perihelion and positive after perihelion. The H_2O production rates deduced from ROSINA are in agreement with the observations of the other instruments on board of Rosetta (Hansen et al. 2016). With the exception of CO at large distances from the nucleus, the four species show a relatively smooth increase up to about 0.3 au before perihelion which corresponds to the heliocentric distance when the comet passed equinox (1.5 au) where the production rate curve shows a steepening. After perihelion, a steady decrease in gas production rate is observed. The maximum production rate is observed to happen about 20 d after perihelion, which is in agreement with the VIRTIS-H observations around perihelion from Bockelée-Morvan et al. (2016).

We can investigate the ratios of the CO_2, CO, and O_2 production rates with respect to H_2O (Fig. 12). While the O_2/H_2O ratio starts by increasing at large heliocentric distances, it stabilizes around its average value of 1.8 per cent. However, both CO_2/H_2O and CO/H_2O show a steep decrease up to a heliocentric distance of ~ 2.6 au. Then, CO/H_2O remains rather close to constant for an average value of 4.6 per cent whereas CO_2/H_2O increases steeply a bit before perihelion and continues to steadily increase hereafter. As the comet goes away from the Sun and continues its journey in the Solar system, we can expect the H_2O production rate to continue decreasing faster than CO_2.

Following a similar procedure, we computed the H_2O and CO_2 gas production rates of comet 67P deduced from the VIRTIS-H observations and our DSMC model. The H_2O production rates de-
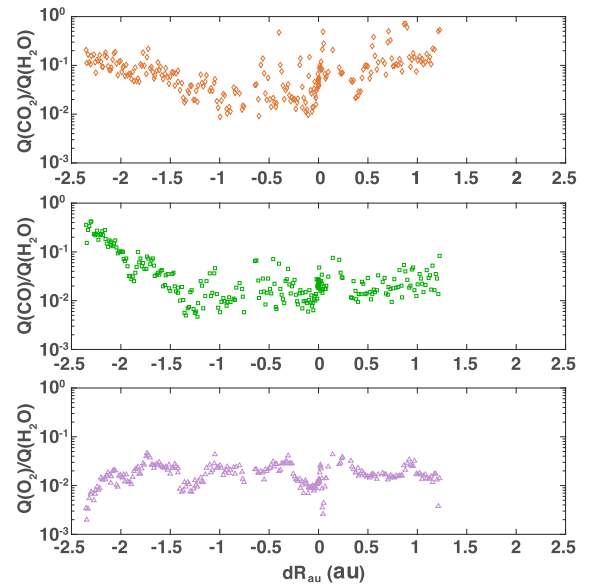

Figure 12. Evolution of the production rate for the ratios CO_2/H_2O (orange), CO/H_2O (green), and O_2/H_2O (purple) from the DFMS data using the DSMC model to take into account the asymmetry of the coma and the evolution of the velocity as a function of heliocentric distance with respect to the closest approach (1.24 au) dR_{au} using the definition that dR_{au} is negative before perihelion and positive after perihelion.

duced from the VIRTIS measurements with a maximum value of $\sim 5 \times 10^{27}$ s^{-1} are smaller than those obtained with the ROSINA observations due to the discrepancy mentioned in Section 4.2. Values computed using the Microwave Instrument for the Rosetta Orbiter (MIRO) data, another remote sensing instrument on board the Rosetta spacecraft, tend to agree with those deduced from the VIRTIS-H observations (Biver, private communication). Indeed, these values can be corroborated using a simple Haser model. We assume that all the H_2O is released by a half sphere (southern latitudes), which should be a good approximation from the observations of Fig. 9 that are comparable to the VIRTIS-H raster images from Bockelée-Morvan et al. (2016). We pick the largest column density from Bockelée-Morvan et al. (2016) on 2015 August 19 at 15:34:33 UT with a value of 1.16×10^{21} m^{-2}. At this time, the pointing and south pole phase angles were 262° and 303°, respectively, which is

close to the Sun direction of $270°$(Bockelée-Morvan et al. [2016]). The pointing distance being 2.97 km (Bockelée-Morvan et al. [2016]), assuming a velocity of 800 m s^{-1} which is in agreement with the velocities obtained with our simulations, this first-order calculation leads to a maximum H_2O production rate of 5.5×10^{27} s^{-1}. These values are somewhat smaller than the H_2O production rates observed during the previous perihelion passages from the full coma (including large distances from the nucleus) of comet 67P. The SWAN instrument on board the SOHO spacecraft observed average H_2O production rates within 15 d after perihelion of 1.3×10^{28} s^{-1}, 1.7×10^{28} s^{-1}, and 5.65×10^{27} s^{-1}, for the 1996, 2002, and 2009, respectively (Bertaux et al. [2014]). This reinforces our hypothesis of the possible presence of an extended source of gas in the coma. Yet, the SWAN observations suggest lower H_2O production rates than the ones deduced from the ROSINA data. Evidence of sublimating icy grains in the coma of 67P may also be present in the OSIRIS cameras' data, notably in images from 2015 May when the comet was at a distance of 1.53 au from the Sun (Gicquel et al. [2016]). The authors proposed an interpretation on reproducing the steep radial brightness profile of a single jet using sublimating dirty aggregates with radii between 5 and 50 μm with an initial mass of water ice of 22 kg (Gicquel et al. [2016]). Such dirty grains deposit water within the first couple of hundreds of kilometres from the nucleus (Fougere [2014]). It seems possible that this mechanism appears more globally in the coma and could partially explain the observations detailed in the present paper.

6 CONCLUSIONS

This work describes the latest effort of coma modelling applied to *in situ* and remote sensing measurements of the Rosetta target comet 67P. The orientation of the nucleus' rotation axis ($52°$) implies a large seasonal effect. Important differences in the coma have been observed before and after the first equinox in late 2015 May. While O_2 stays correlated to H_2O throughout the entire period, CO_2 and CO, which had a poor correlation with respect to H_2O pre-equinox, also became well correlated with H_2O post-equinox. Similarly, the raster images obtained with VIRTIS-H (Bockelée-Morvan et al. [2016]) a few weeks before perihelion show that both H_2O and CO_2 are mostly released from the southern latitudes of the nucleus, while VIRTIS-M images obtained pre-equinox (Migliorini et al. [2016]; Fink et al. [2016]) showed much higher column densities of H_2O close to the 'neck' region of the nucleus.

Following the work done pre-equinox from Fougere et al. ([2016]), we derived the surface activity distribution constraining the model with DFMS data from 2014 August to 2016 February. Both distributions for H_2O and CO_2 are similar to the ones deduced solely with the pre-equinox data, suggesting that the nucleus general activity has not changed and that the differences observed are mainly due to the changes in illumination conditions perhaps combined with long-term evolutionary changes in the nucleus due to the strong seasonal asymmetry.

The DSMC model is able to capture these seasonal changes in the species density variations observed by both ROSINA and VIRTIS. Also, it follows rather well the diurnal variations of these species especially for H_2O and O_2 compared to the DFMS data. A quantitative model comparison with the CO_2 column densities observed around perihelion by VIRTIS-H from Bockelée-Morvan et al. ([2016]) shows good results. While for H_2O the trend is captured by the model, the overall column densities are overestimated by a factor of ~4. A possible explanation could be the potential presence of sublimating

icy grains releasing H_2O at extended distances from the nucleus but a more complete study would be necessary to confirm this.

The evolution of the production rate deduced from DFMS using the DSMC model shows an increase in the production rate curve after equinox for the four species considered in this study, when the Sun starts mostly illuminating the Southern hemisphere of the nucleus. The maximum production rate is reached about 20 d after perihelion as a natural consequence of the changing seasonal solar illumination and the surface distribution of the emission of the major volatile species remaining unchanged over the 18 month period, which is consistent with the VIRTIS observations from Bockelée-Morvan et al. ([2016]).

The surface activity distributions found in this study and the evolution of the production rate with heliocentric distance suggest that in the Northern hemisphere, the long and rather cold summer has enough Sun exposure, which starts as the comet is going away from the Sun during the previous perihelion passage to empty the upper layers of super-volatiles such as CO_2 but not H_2O. This process leaves H_2O as the dominant species in the Northern hemisphere of the nucleus as observed in the 'neck' area. The effect may be enhanced by the fall back of icy material including icy grains lifted from the Southern hemisphere during the short and intense summer (Rubin et al. [2014]). On the other hand, the Southern hemisphere undergoes a short but intense summer, which constantly exposes new material. This suggests that a change in the relative behaviour of the density evolution of the different species should occur again after the second equinox happening in 2016 March with much of the activity shutting down.

REFERENCES

A'Hearn M. F. et al., 2011, Science, 332, 1396

Balsiger H. et al., 2007, Space Sci. Rev., 128, 745

Bertaux J.-L., Combi M. R., Quémerais E., Schmidt W., 2014, Planet. Space Sci., 91, 14

Bieler A. et al., 2015a, Nature, 526, 678

Bieler A. et al., 2015b, A&A, 583, A7

Bird G. A., 1994, Molecular Gas Dynamics and the Direct Simulation of Gas Flows. Oxford University Press, Oxford

Biver N. et al., 2015, A&A, 583, A3

Bockelée-Morvan D., 1987, A&A, 181, 169

Bockelée-Morvan D. et al., 2015, A&A, 583, A6

Bockelée-Morvan D. et al., 2016, MNRAS, 00, 00

Combi M. R., 1996, Icarus, 123, 207

Coradini A. et al., 2007, Space Sci. Rev., 128, 529

Davidsson B. J. R., Gutierrez P. J., 2004, Icarus, 168, 392

Davidsson B. J. R., Gutierrez P. J., 2005, Icarus, 176, 453

Davidsson B. J. R., Gutierrez P. J., 2006, Icarus, 180, 224

Debout V., Bockelée-Morvan D., Zakharov V., 2016, Icarus, 265, 110

De Sanctis C., Lasue J., Capria M. T., Magni G., Turrini D., Coradini A., 2010, Icarus, 207, 341

Feaga L. M., A'Hearn M. F., Sunshine J. M., Groussin O., Farnham T. L., 2007, Icarus, 190, 345

Feldman P. et al., 2015, A&A, 583, A8

Filacchione G. et al., 2016a, Icarus, 274, 334

Filacchione G. et al., 2016b, Science, in press

Fink U. et al., 2016, Icarus, 277, 78

Fougere N., 2014, PhD thesis University of Michigan

Fougere N., Combi M. R., Rubin M., Tenishev V., 2013, Icarus, 225, 688

Fougere N. et al., 2016, A&A, 588, A134

Gicquel A. et al., 2016, MNRAS, 00, 00

Hansen K. C. et al., 2016, MNRAS, 00, 00

Hässig M. et al., 2015, Science, 347, aaa0276

Huebner W. F., Keady J. J., Lyon S. P., 1992, Ap&SS, 195, 1

Johnson E. G., Nier A. O., 1953, Phys. Rev., 91, 10

Keller H. U., Mottola S., Skorov Y., Jorda L., 2015, A&A, 579, L5

Le Roy L. et al., 2015, A&A, 583, A1

Mall U. et al., 2016, ApJ, 819, 126

Migliorini A. et al., 2016, A&A, 589, A45

Mottola S. et al., 2014, A&A, 569, L2

Rubin M., Fougere N., Altwegg K., Combi M. R., Le Roy L., Tenishev V. M., Thomas N., 2014, ApJ, 788, 168

Schläppi B. K. A. et al., 2010, J. Geophys. Res.: Space Phys., 115, A12

Schunk R. W., Nagy A. F., 2009, Ionospheres: Physics, Plasma Physics, and Chemistry. Cambridge University Press, Cambridge, UK, p. 628

Tenishev V., Combi M. R., Davidsson B., 2008, ApJ, 685, 659

Tenishev V., Combi M. R., Rubin M., 2011, ApJ, 732, 104

This paper has been typeset from a TeX/LaTeX file prepared by the author.